AGU PUBLICATIONS

JGR

Journal of Geophysical Research: Solid Earth

RESEARCH ARTICLE
10.1002/2017JB014355

Special Section:
Rock Physics of the Upper Crust

Permeability and seismic velocity and their anisotropy across the Alpine Fault, New Zealand: An insight from laboratory measurements on core from the Deep Fault Drilling Project phase 1 (DFDP-1)

M. J. Allen[1], D. Tatham[1], D. R. Faulkner[1], E. Mariani[1], and C. Boulton[1,2]

[1]Department of Earth Ocean and Ecological Sciences, University of Liverpool, Liverpool, UK, [2]Department of Geological Sciences, University of Canterbury, Christchurch, New Zealand

Key Points:
- Low permeability and seismic velocity is associated with the damage zone of the Alpine Fault Zone, New Zealand
- The development of pervasive gouge-filled and calcite-filled fractures explains the low permeability and seismic velocity
- Seismic velocity anisotropy is low (<30%) due to the lack of preferred orientation of the fracture network in the fault damage zone

Supporting Information:
- Supporting Information S1
- Table S1
- Table S2
- Table S3
- Figure S1
- Movie S1
- Movie S2

Correspondence to:
M. J. Allen,
mjallen@liverpool.ac.uk

Citation:
Allen, M. J., D. Tatham, D. R. Faulkner, E. Mariani, and C. Boulton (2017), Permeability and seismic velocity and their anisotropy across the Alpine Fault, New Zealand: An insight from laboratory measurements on core from the Deep Fault Drilling Project phase 1 (DFDP-1), *J. Geophys. Res. Solid Earth*, *122*, 6160–6179, doi:10.1002/2017JB014355.

Received 25 APR 2017
Accepted 17 JUL 2017
Accepted article online 20 JUL 2017
Published online 19 AUG 2017

©2017. The Authors.
This is an open access article under the terms of the Creative Commons Attribution License, which permits use, distribution and reproduction in any medium, provided the original work is properly cited.

Abstract The Alpine Fault, a transpressional plate boundary between the Australian and Pacific plates, is known to rupture quasiperiodically with large magnitude earthquakes (M_w ~8). The hydraulic and elastic properties of fault zones are thought to vary over the seismic cycle, influencing the nature and style of earthquake rupture and associated processes. We present a suite of laboratory permeability and *P* (V_p) and *S* (V_s) wave velocity measurements performed on fault lithologies recovered during the first phase of the Deep Fault Drilling Project (DFDP-1), which sampled principal slip zone (PSZ) gouges, cataclasites, and fractured ultramylonites, with all recovered lithologies overprinted by abundant secondary mineralization, recording enhanced fluid-rock interaction. Core material was tested in three orthogonal directions, orientated relative to the down-core axis and, when present, foliation. Measurements were conducted with pore pressure (H_2O) held at 5 MPa over an effective pressure (P_{eff}) range of 5–105 MPa. Permeabilities and seismic velocities decrease with proximity to the PSZ with permeabilities ranging from 10^{-17} to 10^{-21} m^2 and V_p and V_s ranging from 4400 to 5900 m/s in the ultramylonites/cataclasites and 3900 to 4200 m/s at the PSZ. In comparison with intact country rock protoliths, the highly variable cataclastic structures and secondary phyllosilicates and carbonates have resulted in an overall reduction in permeability and seismic wave velocity, as well as a reduction in anisotropy within the fault core. These results concur with other similar studies on other mature, tectonic faults in their interseismic period.

1. Introduction

The quantitative characterization of the physical properties of fault zones, such as permeability and the transmission of seismic waves, is essential in order to understand the influence they have on fluid flow and seismicity in the brittle crust. Upper-crustal fault zones can be divided into three primary components: the fault core, the damage zone, and the host protolith. These components may be lithologically and structurally distinct and vary in proportion according to geological setting [*Chester and Logan*, 1986; *Caine et al.*, 1996; *Faulkner et al.*, 2010]. The fault core can consist of singular or multiple anastomosing slip surfaces and is where the highest strain and most displacement are accommodated [*Faulkner et al.*, 2003]. This core is usually nested within a damage zone, a region of kinematically related cracks and small faults, decreasing in density with distance from the core and transitioning into the local host protolith [*Anders and Wiltschko*, 1994; *Wilson et al.*, 2003; *Mitchell and Faulkner*, 2009].

The Alpine Fault in New Zealand is a major fault that forms the active plate boundary between the Pacific and Australian plates. The exhumation of the Alpine Fault hanging wall enables us to make direct observations of the internal structure of a large plate-boundary fault, which is late in its seismic cycle and could therefore provide important information on the fault state at the time prior to an earthquake. The damage zone of the Alpine Fault of New Zealand is composed of diverse fault rock lithologies including clay-rich gouges, cataclasite, ultramylonites, and fault breccias, all overprinted, to different extents, by a geochemically altered zone, which, in this fault, masks evidence of a brittle-viscous transition [*Sibson et al.*, 1981; *Caine et al.*, 1996; *Sutherland et al.*, 2012].

Fault zone architecture has a considerable influence on the hydraulic properties of the rock surrounding fault zones, with faults acting as either conduits or barriers for fluid flow or a combination of the two [*Caine et al.*,

1996; *Evans et al.*, 1997]. The determining factors are dominantly the ratio of fault core (typically low permeability regions) to damage zone (high permeability regions), with the fault core acting as a barrier to flow across the fault and the damage zone acting as a conduit for fault-parallel flow [*Caine et al.*, 1996]. Furthermore, there may be inherent anisotropy within the rocks of both the fault core [*Faulkner and Rutter*, 1998; *Farrell et al.*, 2014] and the damage zone [*Faulkner and Armitage*, 2013]. This model is further complicated by the occurrence of fault-related alteration via fluid-rock interactions. This commonly leads to phase transformation, clay mineral generation, and cementation and hence variations in physical properties with time [e.g., *Wintsch et al.*, 1995; *Holdsworth*, 2004].

Investigation at a variety of scales requires quantification of the variables that control fault zone behavior, for instance, whether slip is accommodated seismically or aseismically, whether a fault is a fluid conduit or barrier, can pore fluid overpressures develop, or will mineralization occur. Geophysical investigation techniques, such as seismic and electrical resistivity surveys, give broad regional information on fault structure [e.g., *Rietbrock*, 2001; *Eberhart-Phillips and Bannister*, 2002; *Hoffmann-Rothe et al.*, 2004; *Lay et al.*, 2016]. Direct observations of fault zones, and collection of samples for laboratory testing and microstructural analyses, are limited to faults that have been exhumed to the surface [e.g., *Wibberley and Shimamoto*, 2002] or that have been drilled and cored at depth [e.g., *Zoback et al.*, 2011]. Otherwise, only indirect measurements of some of the properties of faults at depth are possible through inference [e.g., *Faulkner et al.*, 2008; *Mitchell and Faulkner*, 2012].

In this paper, laboratory measurements of permeability and ultrasonic wave velocity are made on fault rock samples recovered from the central Alpine Fault Zone. These specimens were sampled from core collected from two shallow (<150 m depth) boreholes that were drilled as part of the Deep Fault Drilling Project (DFDP-1). These cores provide a unique opportunity to sample through a continuous section across the Alpine Fault Zone, uninterrupted by thick vegetation and relatively unaffected by surface weathering effects. First, a brief introduction to the Alpine Fault Zone and the DFDP project is given. Then the techniques used to prepare the delicate samples analyzed are described. Finally, results of permeability, *P* and *S* wave velocity measurements, including their anisotropy, and microstructural controls are described, and their influence on fault zone processes during and after seismicity is discussed.

1.1. The Alpine Fault, New Zealand, and DFDP Drilling

The Alpine Fault Zone (AFZ), bounding the western edge of the Southern Alps on New Zealand's South Island, accommodates over 70% of the relative motion between the colliding Australian and Pacific Plates [*Norris and Toy*, 2014]. The ramping of the Pacific plate over the Australian plate is accommodated through dextral-reverse movement, offsetting basement rocks laterally by ~470 km, with Quaternary horizontal displacement rates estimated at 21–27 mm yr^{-1} [*Norris and Cooper*, 2001; *Lamb et al.*, 2015]. Uplift across the fault is rapid, exhuming crustal rocks from depths of 20–30 km at a rate of ~6–9 mm yr^{-1} [*Little et al.*, 2002]. Accompanying this rapid uplift is the advection of the regional geothermal gradient. Quartz fluid inclusion microthermometry places the gradient at 40°C/km [*Toy et al.*, 2010], while titanium thermobarometry of quartz shows a gradient of 45°C/km [*Cross et al.*, 2015] and recent shallow borehole measurements report gradients of 62.6 ± 2.1 and 125 ± 55°C/km [*Sutherland et al.*, 2012, 2017].

Palaeoseismic evidence indicates that the Alpine Fault has had numerous geologically recent rupture episodes at 1717, 1620, and 1430 A.D., estimated to have moment magnitudes of 7.9 ± 0.3, 7.6 ± 0.3, and 7.9 ± 0.4, respectively [*Langridge et al.*, 2012]. This, coupled with recent seismicity patterns, geodetic strain records, and regional low-velocity zones indicative of high pore fluid pressures deep in the fault zone, suggests that the fault is locked above 6–12 km depth and is in the late stage of the earthquake cycle [*Eberhart-Phillips*, 1995; *Sutherland et al.*, 2007; *De Pascale and Langridge*, 2012; *Lamb and Smith*, 2013]. The global significance of the Alpine Fault in the study of major fault zones and crustal processes is considerable; the opportunity to study a locked continental plate boundary fault thought to be late in the earthquake cycle will yield insight into the prerupture conditions of a major fault and the nature of the interseismic physicochemical processes that have taken place.

The Deep Fault Drilling Project (DFDP) was undertaken to understand better the processes that lead to major earthquakes by drilling into and observing a major continental fault during its buildup to a large seismic event. The first phase of the Deep Fault Drilling Project (DFDP-1) comprised two pilot holes (DFDP-1A and DFDP-1B) drilled into an active thrust segment of the AFZ at Gaunt Creek, Westland, in January 2011

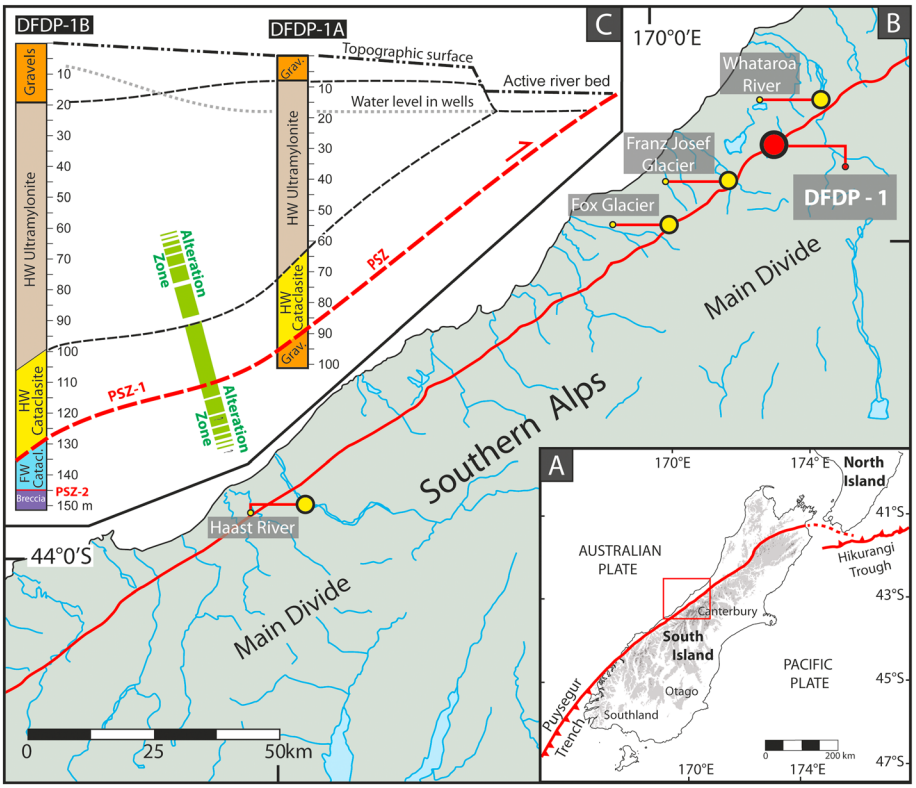

Figure 1. (a) Location of the Alpine Fault Plate Boundary across the continental New Zealand, South Island. Topography shading, light grey >800 m and dark grey >1800 m. The red box shows the (b) central region of the Alpine Fault; the location of DFDP-1 is shown in the red circle. (c) Cross section of DFDP-1 boreholes showing schematic lithological divisions and local topography, adapted from *Sutherland et al.* [2012]. HW = hanging wall, FW = footwall.

(Figure 1). The boreholes reached depths of 100.6 and 151.4 m, respectively, sampling a range of fault lithologies including ultramylonites, cataclasites, and gouges. All samples used in this study were collected from core recovered from DFDP-1A and 1B. The principal slip zone (PSZ) of the AFZ was reached at 90.74 m depth in DFDP-1A and 128.44 m in DFDP-1B, marking the boundary between the Australian and Pacific Plates, with a second PSZ within footwall rocks recorded in DFDP-1B at 144 m. The PSZ in both boreholes is composed of clay-rich gouge (Figure 1) [*Sutherland et al.*, 2012].

Drilling revealed the presence of a ~30 m thick alteration zone overprinting both the fault core and damage zone. This "alteration zone" was defined based on a distinctive light green color in core and in outcrop produced by elevated concentrations of alteration minerals (e.g., phyllosillicates and carbonates) above regional levels [*Sutherland et al.*, 2012; *Townend et al.*, 2013; *Toy et al.*, 2015; *Boulton et al.*, 2017]. The degree of alteration increases with proximity to the PSZ within the fractured ultramylonites and cataclasites of the damage zone, implying that extensive fluid-rock interactions have occurred in the hanging wall of the Alpine Fault.

2. Methods

2.1. Sample Selection and Preparation

For this study, samples were collected from both the DFDP-1A and 1B drill cores. The drilled core diameter was 85 mm (PQ wireline bit size) and supplied for sample preparation as 200–300 mm length intact core rounds and half rounds. These core sections were axially oriented to the borehole axis, however, due to core rotation during retrieval the azimuthal orientation, could not be preserved [*Sutherland et al.*, 2011; *Toy et al.*, 2015]. The lithological character of the recovered core has been described in detail by *Toy et al.* [2015]. The core (and consequently the fault zone) was classified into a number of lithological units, based on the original protolith and level of damage/alteration. These unit classifications are outlined in Figure 2. Seven hanging wall cataclasites (Units 3 and 4), two footwall cataclasites (Units 6a and 6b), and the PSZ gouge were

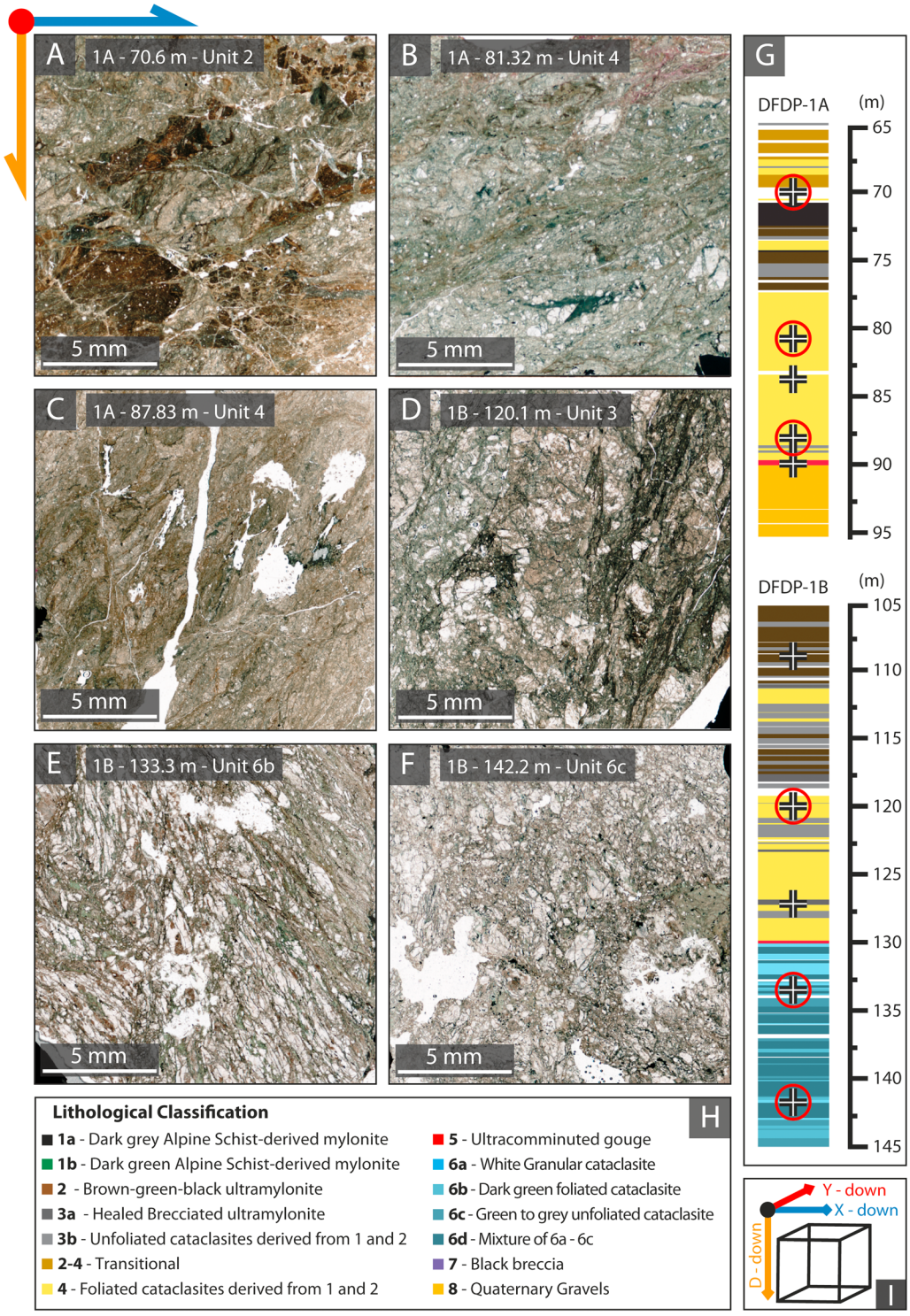

Figure 2. Photomicrographs of cataclastic microstructures from the (a–d) hanging wall and the (e and f) footwall of the Alpine Fault from both DFDP-1A and 1B drill cores. The blue/red/orange direction arrows denote the direction of measurement used in Figures 5 and 6. (g and h) The classification scheme is adapted from *Toy et al.* [2015]. The crosses in Figure 2g represent regions of sampling in the drill core; the red circle denotes the location of pictured cube micrographs (Figures 2a–2f).

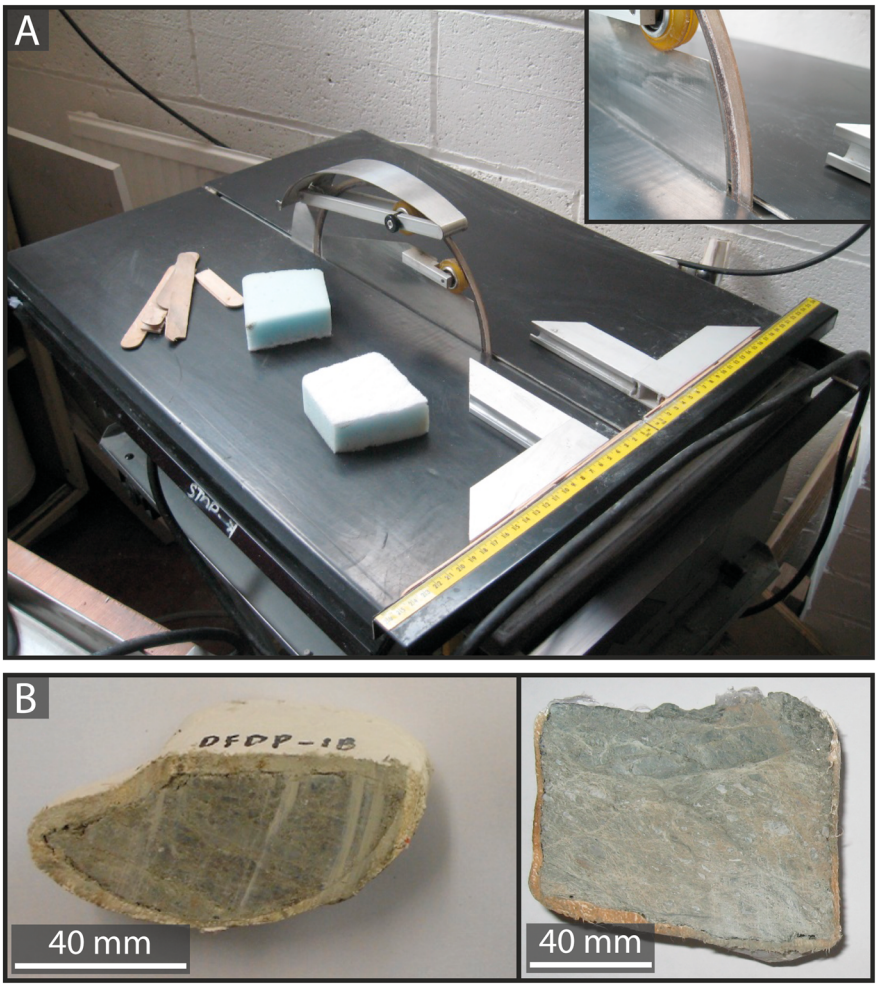

Figure 3. (a) The Revolution XT Ring Saw, developed by Gemini Saw Company, used in shaping the test specimens. (b) Examples of clean cut surfaces of cataclasites bound in ModRoc® bandages.

sampled in this study, representing a section across the plate boundary (Unit 5). For comparison, lithologies classified as potential protoliths for the Alpine Fault cataclasites were collected from the field and tested. These include an Alpine Schist, a foliated quartzofeldspathic schist, and a quartzofeldspathic ultramylonite all collected from the fault's hanging wall exposures in the Southern Alps foothills close to the drill site. For more details on these lithologies, see *Cooper* [1972] and *Little et al.* [2015], respectively. Most hanging wall cataclasites used in this study were sourced from the alteration zone (see *Sutherland et al.*, 2012), a zone of heavily altered cataclasites rich in carbonate precipitation and authigenic phyllosilicates (illite/muscovite and chlorite). Figure 2 depicts selected optical micrographs of the tested material and a schematic outlining core sampling intervals.

Due to the friable nature of many of the test specimens, traditional methods of sample preparation such as water-lubricated coring, sawing, and grinding proved catastrophic, causing washout of the finer grain-size fractions and often total disaggregation. We therefore developed new, reliable preparation techniques to produce systematically intact samples suitable for experimental investigation. The aim was to produce cubic samples that could be used for measurements of anisotropy of both permeability and ultrasonic wave velocity.

Initially, the core was wrapped in thin plastic wrap followed by the application of three to four layers of ModRoc® (gypsum plaster bandages). The original core orientation was recorded throughout the wrapping process, and once fully hardened, it was scribed onto the final plaster covering. Cutting the material was accomplished through the use of an annular saw (Revolution XT Ring Saw; Figure 3). The configuration of

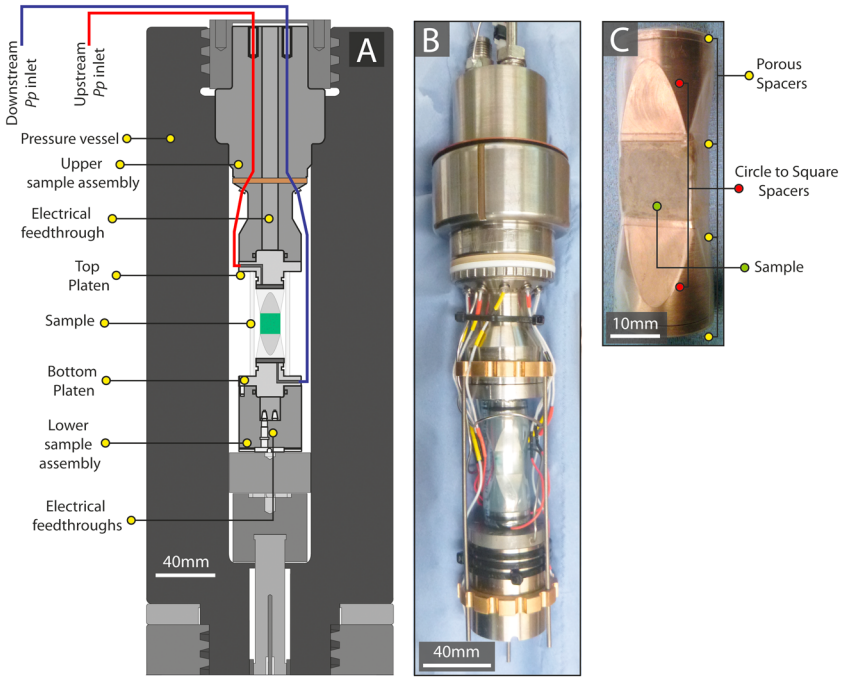

Figure 4. (a) Schematic illustration of the triaxial experimental apparatus used in the study, including the seismic sample assembly housed within the pressure vessel. (b) The seismic sample assembly with piezoelectric ceramics and pore fluid supply pipes set into the upstream and downstream platens. (c) A cube-shaped specimen set between porous steel spacers (both square and circle) and a circle to square adapter to allow coupling with the circular assembly platens.

the annular blade means that only the actively cutting portion of the blade is in contact with the sample. This reduces grain plucking and disaggregation. Some cooling and lubricating fluid (water in this case) is required during cutting; this was applied by gently pressing a moist sponge to the blade edge.

After each cut, the exposed face was again covered by plastic wrap and ModRoc® following the above procedure and repeated until a ~15 × 15 × 15 mm cube was produced. The final cube is orientated to the vertical borehole axis, with two orientations orthogonal to the core cut according to any microstructural fabric if present, i.e., foliations, calcite veins, and fractures. A final step, if the specimen proved sufficiently robust, involved hand grinding the cube surfaces with dry, fine emery paper to provide a smooth flat surface to maximize acoustic wave and fluid transmission from the sample assembly to the sample cube. Once preparation was complete, the specimen, porous steel spacers, and solid steel spacers were jacketed in heat-shrink polyolefin in order to secure the sample. This was then jacketed in PVC tubing, which forms a physical barrier between the sample and its pore fluid, and the silicon oil confining medium (Figure 4).

Once measurements were concluded, the experimental specimens were prepared for microstructural analysis, with their orientations preserved, using standard petrographic thin section techniques if the samples were sufficiently robust. Friable material was prepared by using "water-free" polishing techniques by Paul Hands of Hand On Thin Sections Ltd. As the DFDP core is not horizontally oriented, the relative orientation of the observed microstructures cannot be conclusively related to the fault orientation.

2.2. Experimental Procedure

The triaxial experimental apparatus used to undertake permeability and seismic velocity measurements is illustrated schematically in Figure 4 [*Faulkner and Armitage*, 2013]. During each experiment, the sample assembly was loaded into the pressure vessel, confining pressure (P_c) of 10 MPa was applied using a low-viscosity silicon oil confining medium, and finally, the specimen was allowed to saturate with deionized water pore fluid, which was allowed to equilibrate at a pore fluid pressure (P_f) of 5 MPa and an effective confining pressure (P_e) of 5 MPa, assuming a simple effective pressure law where the poroelastic constant α is equal to unity [*Rice and Cleary*, 1976]. Confining pressure and pore fluid pressure are servo-controlled to a resolution of ≤0.1 MPa.

Since each sample was recovered and tested again 3 times in three orthogonal orientations (*x*, *y*, and *z*, see Figure 2i), no measurements were recorded during the first pressure cycle each sample experienced. A pressure cycle consisted of increasing the confining pressure through the range 10, 20, 35, 45, 60, 70, 85, 95, and 110 MPa, while holding the P_f at 5 MPa. These effective pressures (P_{eff} = 5, 15, 30, 40, 55, 65, 80, 90, and 105 MPa) are approximately equivalent to pressure conditions spanning the near surface to ~5–6 km depth. This method means that, during an experiment, the samples were overconsolidated with respect to the near-surface conditions, removing the effects of sample preparation, storage, transport, and the effect of unloading during retrieval between tests on the same sample, making comparison with borehole measurements difficult. Another consideration to be made is the evolution of the fault rocks during the exhumation of the Alpine Fault. As mentioned above, the Alpine Fault is a mature fault that has undergone extensive and cyclical comminution and geochemical alteration. Consequently, the specimens tested are likely to be substantially different structurally and compositionally to fault rocks at depths of ~5–6 km. Nonetheless, the results provide insight and an approximation of the permeability and seismic velocity of the Alpine Fault as it is exhumed from depth.

Piezoelectric ceramic transducers (piezoelectric lead zirconate titanate 5H, fundamental frequency at 1.5 MHz), with *P* wave and orthogonal *S* wave polarization directions, are housed in each opposing platen and are used to produce and record ultrasonic *P* and *S* waves through the samples. The ultrasonic velocities are measured using the through-transmission method, utilizing the travel times and specimen length [*Birch*, 1960] after correction for the travel time through the loading platens. Elastic wave speeds were picked and velocities calculated over an effective pressure range of 55–105 MPa for *S* waves (V_s) and 15–105 MPa for *P* waves (V_p). Poor coupling between the loading platens and the test specimen at low effective pressures ($<$55 MPa for V_s and $<$15 MPa for V_p) made reliable picking of arrival times difficult, and so these data are not reported.

Permeability measurements were performed using the pulse transient technique [*Brace et al.*, 1968], involving the introduction of small pressure difference of $<$1 MPa to one end of the specimen and observing the pressure decay through the sample with time. One effective pressure cycle consisted of measuring the permeability, V_p and V_s at each effective pressure as the confining pressure is increased, with the unloading effective pressure path covering the same increments during measurement. A typical pressure cycle lasted between 3 and 7 days owing to the low permeability of some samples. Once one pressure cycle was completed for a given cube orientation, the specimen was removed from its jacket and reoriented and the above experimental procedure was repeated.

In a typical experiment, permeability and seismic velocities do not fully recover after deconfinement from the initial up-pressure leg, with upleg and downleg variations typically an order of magnitude for permeability and between 2 and 30% for seismic velocities; see Figure S1 in the supporting information for an illustration of this hysteresis. Subsequent variations after repeated pressure cycles become progressively smaller. Similar procedures and observations are reported by *Bernabe* [1987], *Faulkner and Rutter* [2000], and *Morrow et al.* [2014]. The drying and unloading of samples at room conditions were minimized by conducting experiments for each sample orientation in immediate succession or by sealing the sample in heat shrink or plastic film where this rapidity was not possible.

As these samples have undergone compaction and consolidation up to pressures of 105 MPa, the measurements do not correlate with borehole wireline and slug tests but rather reflect greater depths on the Alpine Fault. We refer to *Carpenter et al.* [2014] for experimental results performed at in situ borehole conditions.

3. Results

3.1. Permeability Measurements

Permeability results are plotted as log permeability against effective pressure and show a systematic decrease with increasing P_{eff}, generally decreasing by larger increments over the lower P_{eff} range, ~5–40 MPa, presumably as handling/drilling-induced fractures close. This initial closure can account for a drop in permeability of up to 2 orders of magnitude (for example, the permeability trace for 1A-83.2 in Figure 5c); however, this effect more commonly manifests itself as a drop of 1 order of magnitude. Once above ~30 MPa P_{eff}, the rate of permeability reduction with effective pressure, in most cases, lessens with increasing pressure.

At P_{eff} 5 MPa, permeabilities range from 1.49×10^{-17} m^2 in 1A-81.32 (D-down) to 1.35×10^{-20} m^2 in 1B-127.3 (*X*-down). At P_{eff} 105 MPa, the overall permeabilities range from 1.35×10^{-18} m^2 in 1A-81.32 (*Y*-down) and 1.25×10^{-21} m^2 in 1B-127.3 (*X*-down). In some instances, pressure sensitivity accounts for a greater variation in permeability than individual specimen variation, as shown by 1B-120.1 (D-down) and 1A-83.2 (*Y*-down) in Figures 5a and 5c.

Permeability variation and an indication of the permeability anisotropy throughout the boreholes are illustrated in Figure 6, showing the range of permeabilities of each orientation with variation in P_{eff}. With increasing proximity to the PSZ, permeability decreases. This trend is particularly noticeable in Figure 6a within the hanging wall alteration zone. This same feature is not as easily observed in Figure 6d, within the DFDP-1B core, as sparser sampling density makes it more difficult to highlight the trend, particularly close to the PSZ. Within the DFDP-1B alteration zone, there is a decrease in permeability with depth, and the lowest permeability value of 1.25×10^{-21} m^2 was measured immediately above the PSZ. With increased distance from the PSZ, into the footwall cataclasites (e.g., 1B-142), permeability increases by up to 2 orders of magnitude from ~10^{-20} to ~10^{-18} m^2, respectively (see Figure 6d). Permeability measurements for the "protolith" lithologies could not be performed as their permeability was too low for the resolution of the experimental apparatus, at ~10^{-22} m^2. At permeabilities lower than ~10^{-21} m^2, flow rates are very small and pores are inferred to be approaching molecular size. The permeability anisotropy exhibited by borehole specimens appears to have little correlation to orientation; this is conceivably due to the highly variable microstructures present in these fractured or comminuted lithologies. Direct correlation of permeability with specific microstructural causes is difficult to make, except in the case of 1A-90.67, the clay-rich PSZ gouge. This specimen exhibits the lowest permeability anisotropy at 40%, potentially due to its finer grained and more homogenous structure in comparison to other fault core lithologies.

3.2. Seismic Velocity Measurements

Elastic wave transmission through the specimens shows a similar relation to increasing P_{eff} as permeability, with a rapid increase in velocity over initial pressure increments (e.g., 5 to 40 MPa) stabilizing once open fractures and porosity are reduced at high P_{eff} (~ 40–50 MPa). Both V_p and V_s show similar trends across the fault; the material exhibiting the highest V_p and V_s is on the periphery of the pervasive alteration zone, farthest from the PSZ (1B-108.2 and 1B-120.1), with V_p of ~5700 m/s and V_s of ~4000 m/s (see Figures 6b–6f).

Both V_p and V_s decrease with increased proximity to the PSZ with a substantial reduction in velocity within the PSZ at 1A-90.67. Across the respective pressure ranges, hanging wall V_p values span 4500–5900 m/s with V_s values between 2400 and 4000 m/s. Material from the footwall exhibits lower velocities than the hanging wall with V_p values ranging from 4400 to 5600 m/s and V_s values from 2200 to 3500 m/s. PSZ material exhibits the lowest V_p from 3900 to 4200 m/s and V_s at 1900 to 2000 m/s. Figures 6g and 6h show seismic velocity measurements for the "protolith" lithologies, with the Alpine Schist V_p from 4800 to 6700 m/s and V_s at 3400 to 4250 m/s, while the ultramylonite had V_p of 5600 to 6170 m/s and V_s 3600 to 4030 m/s.

Performing measurements parallel to the down core axis and in two further mutually orthogonal orientations allowed the seismic velocity anisotropy present in these rocks to be investigated and approximated. As only three orientations were measured in this study and these directions are not necessarily oriented parallel to the principal axes of the dynamic elasticity tensor, our measurements provide only a minimum constraint on anisotropy. Figure 7 illustrates the magnitude of this anisotropy with depth at 105 MPa, with the anisotropy calculated using Equation (1) following *Mainprice and Humbert* [1994],

$$AV_{p,s1,s2} = \left(\frac{V_{p,s1,s2}\ \max - V_{p,s1,s2}\ \min}{\overline{V_{p,s1,s2}}} \right) \times 100 \quad (1)$$

where $V_n$max and $V_n$min are the maximum and minimum seismic velocities at a given P_{eff} increment with the subscript n denoting the wave type, while $\overline{V_n}$ is the averaged velocity (0.5 ($V_n$max + $V_n$min) and AV_n is the value of anisotropy in percent.

The degree of anisotropy present in the test specimens appears far greater for permeability than for seismic wave velocity. Presumably, this is largely due to the maintenance of interconnected voids and fractures for

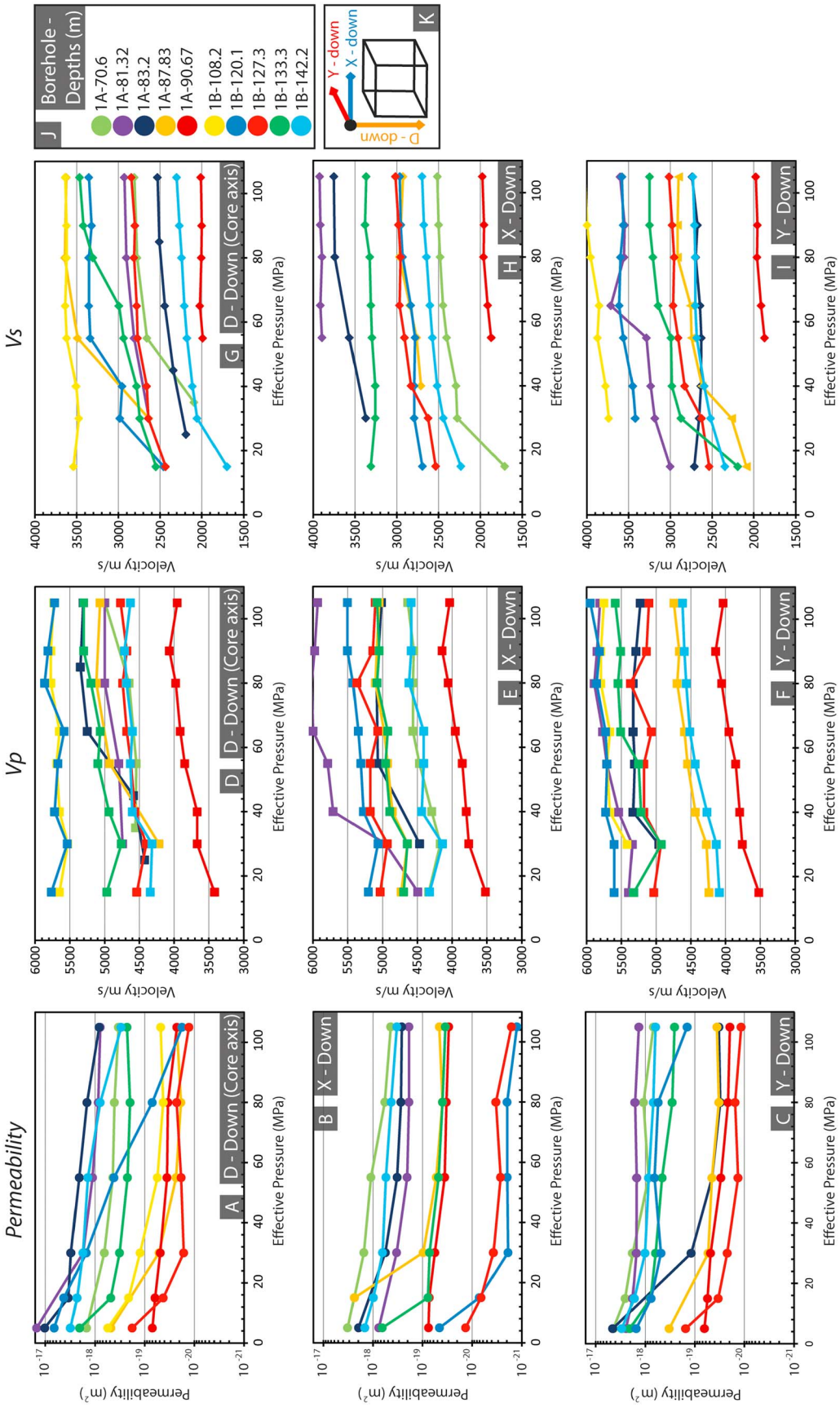

Figure 5. (a–c) Permeability, (d–f) *P* wave velocity, and (g–i) *S* wave velocity measurements as a function of effective pressure. (j) The colors represent depths and are noted in the legend. (k) Each row denotes the orientation of the specimen. D-down is equivalent to the down core axis, while *X*-down and *Y*-down represent two horizontal directions in the borehole; note that the *X* and *Y* directions do not correlate between specimens due to the inability to horizontally orient samples from the drill core.

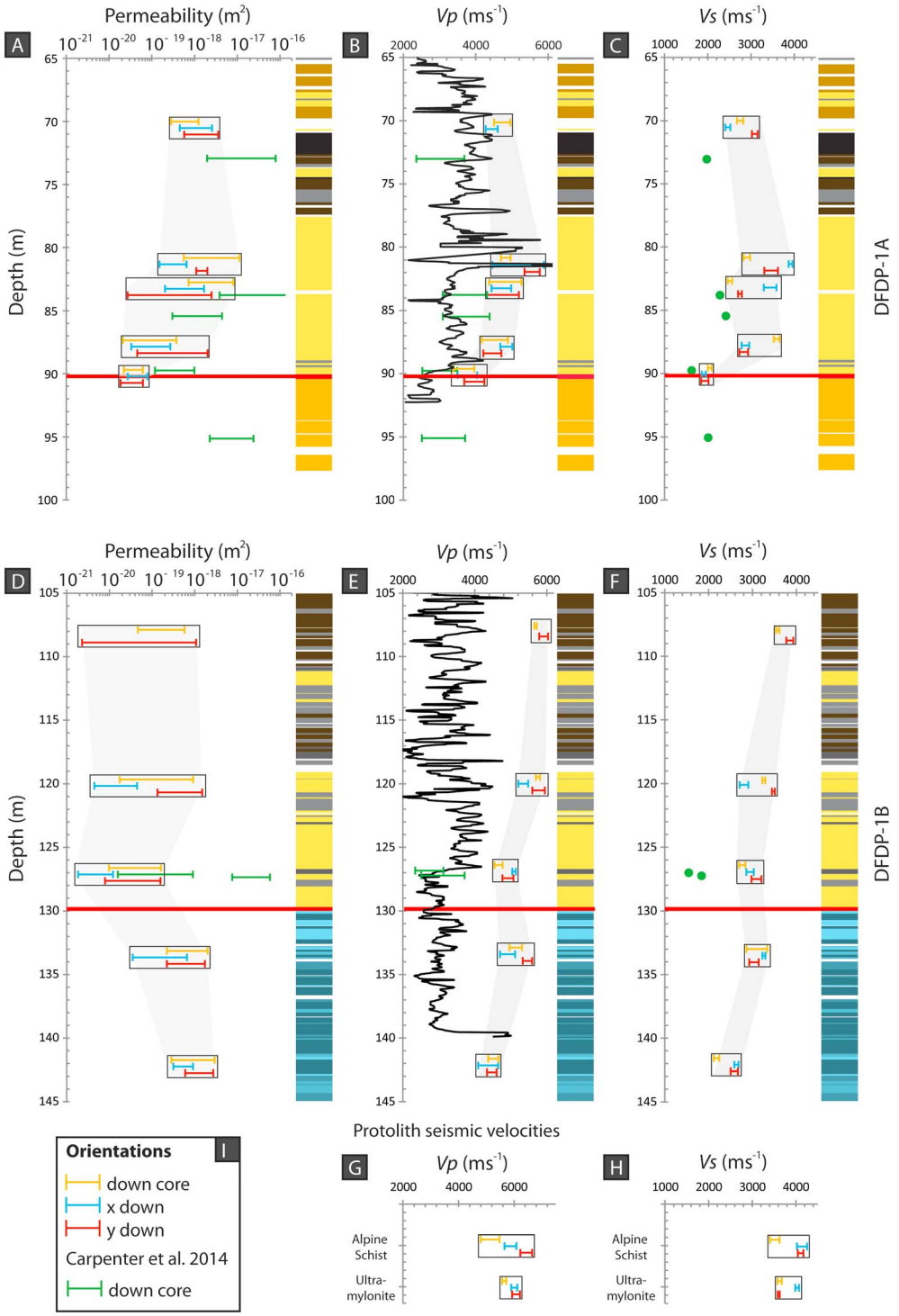

Figure 6. (a–i) Permeability and seismic velocity ranges for material from DFDP-1A and DFDP-1B with depth, including field derived protolith lithologies (Figures 6g and 6h). Each tested specimen is represented by a bar color coded to orientation (see Figure 6i); note that the *X* and *Y* directions do not correlate between specimens due to the inability to horizontally orient samples from the drill core. P_{eff} ranges for permeability measurements are 5–105 MPa, V_p 15–105 MPa, and V_s 55–105 MPa. P_{eff} range for measurements from *Carpenter et al.* [2014] at 2.5–65 MPa. Wireline sonic velocity logs from Figures 6b and 6e are adapted from *Townend et al.* [2013].

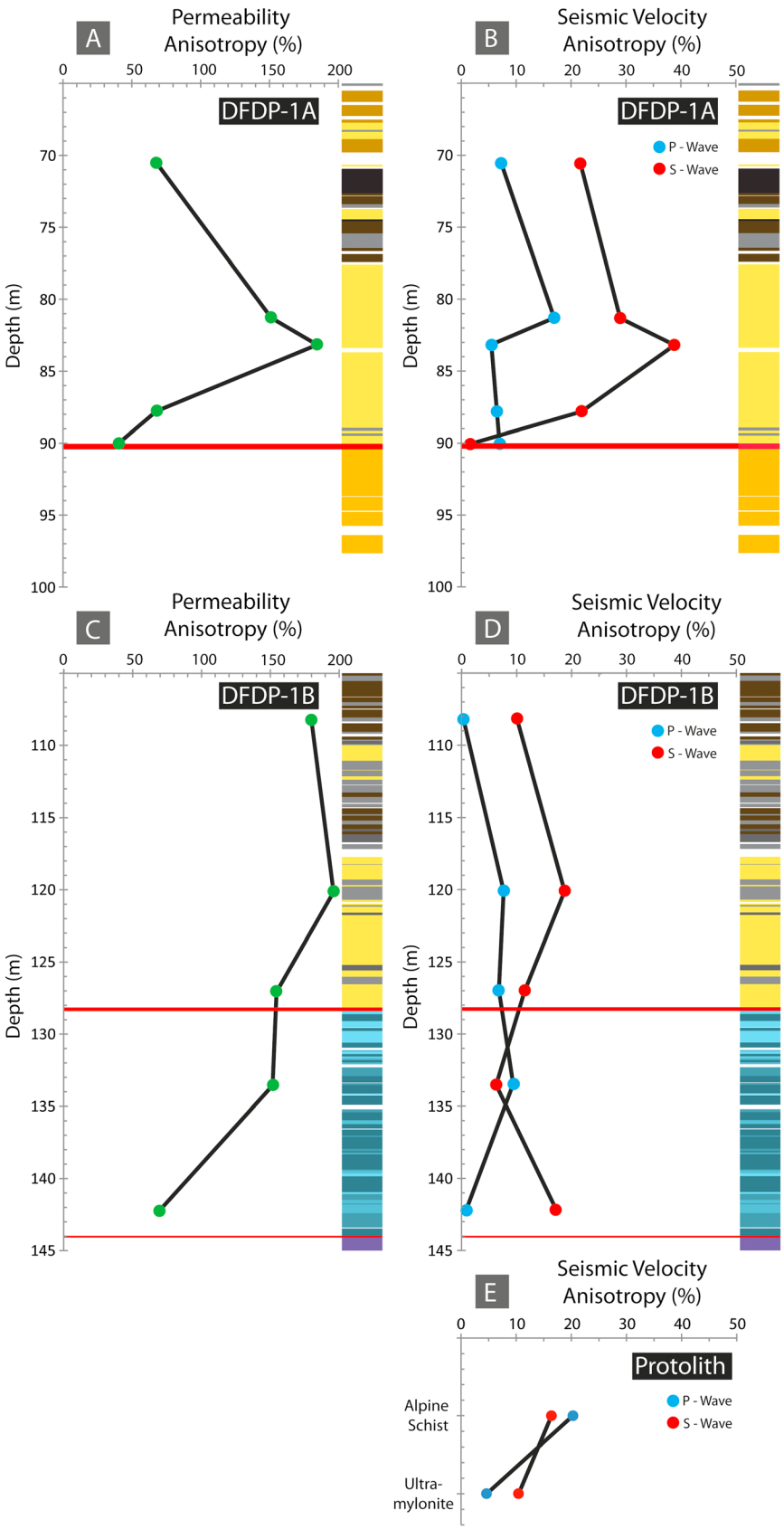

Figure 7. (a and c) Permeability and (b and d) seismic velocity anisotropy with depth at 105 MPa is shown.

fluid mobility, which will be greatly affected by increasing P_{eff}, while the propagation of elastic waves is not limited by fracture/void connectivity in the same way. Similar observations were made by *Fortin et al.* [2011] when hydrostatically loading fractured basalt. We must also state that the anisotropies measured in this study, due to the arbitrary horizontal directions of the test specimens, are a minimum value of transverse anisotropy.

In most specimens, most notably in 1A-83.2 and 1B-142.2, V_{s1} anisotropy is much greater than that found for V_p, potentially due to attenuation as an *S* wave pulse will be more sensitive to scattering of wave energy via impingement on an inhomogeneity, potentially a pore, fracture, foliation, or lithological interface [*Sato et al.*, 2012]. This may explain the 33 and 17% difference in the anisotropy in 1A-83.2 and 1B-142.2, respectively. 1A-83.2 contains a penetrative foliation that may allow for easier transmission of *P* waves, while the *S* waves are more inhibited by the aforementioned factors, particularly pores and fractures. However, 1B-142.2 has no obvious mineral or fracture alignments, implying that the heterogeneity in clast size, shape, and orientation may also result in a greater variation of V_s with orientation than with V_p. Saturation of the fractures present may also be an important influence on seismic wave velocity, particularly in regard to the anisotropy observed. In this study we can assume that the fractures are fully saturated, explaining the greater anisotropy seen in *Vs* than in *Vp*; if anisotropy was greater in *Vp*, this would imply that fractures remained dry throughout the experiments [*Guéguen and Sarout*, 2011].

3.3. Specimen Microstructural Variation

Figure 2 shows the mm- to cm-scale microstructures that govern the variation of physical properties throughout the Alpine Fault damage zone in both the hanging wall and footwall. Gouge-filled fractures are common throughout the alteration zone, generally manifesting as low-displacement shears filled with unconsolidated gouge material of the same composition as adjacent wall rock with little authigenic clay, appearing as angular to subangular shaped clasts ranging from sub-μm to 100 μm diameter (Figure 8c). Occasionally, elongated clasts show a preferred orientation parallel to the vein walls (Figure 8e). These fractures are typified by their lack of carbonate cementation or phyllosilicate alteration and assumingly belong to a relatively recent episode of deformation. Fracture density through the Alpine Fault's damage/alteration zone was quantified by *Williams et al.* [2016] using CT scans of the DFDP-1 core material, reporting that damage zone structures (including open, healed, and semihealed fractures) do not increase in density with proximity to the PSZ, remaining largely uniform throughout the cored interval of the fault. The distribution of these fractures and the presence of authigenic clay minerals within them are the key controlling factors governing the permeability and seismic velocity variations of these rocks. NanoCT scans of specimens from this study are included in Videos S1 and S2 in the supporting information; these images highlight the presence of throughgoing open fractures with little evidence of shear, particularly visible in 1B-120.1 and fractures that contain gouge material visible in 1B-133.3. Cataclasites in the hanging wall are generated from an amphibolite-facies quartzofeldspathic or metabasic mylonitic protolith and are typified by a pervasive carbonate infill, as both cement and vein precipitation, composing of ~5% of the bulk mineralogy. Veining is evidently multigenerational, exhibiting cross-cutting relationships, varying orientations (Figure 2), and evidence of reactivation shown by crack-seal structures. Foliation, when present, is typified by alternating phyllosilicates or opaque oxides anastomosing around sub-mm relict protolith quartz fragments.

In contrast, the footwall cataclasites contain far less carbonate veins and, as a result, are far more incohesive and generally exhibit a lighter grey-white color owing to their prehnite-pumpellyite to greenschist-facies granitic protolith [*Toy et al.*, 2015]. Foliation is similarly variable in pervasiveness, from distinct as in 1B-133.3 (Figure 2e) with obvious alternating quartz/feldspar and phyllosilicate fabric, to completely absent as in 1B-142 (Figure 2f). Foliation is seen to be highly variable in orientation on the sub-cm scale. In contrast with both cataclasites, the PSZ ultracomminuted gouge has a finer grain size ($<$10 μm) and consists of two main gouge types that occur in discrete layers ~30–50 mm thick: a brown smectitic gouge and a blue chloritic/micaceous gouge, described in detail by *Boulton et al.* [2014], the latter of which was tested in this study.

Overall, the mineralogy across the fault, in both the hanging wall and footwall, remains largely constant. X-ray diffraction results from *Boulton et al.* [2017] show that calcite, precipitated as cements and veins, vary in proportion more than any other mineral phase, comprising ~5% of the modal mineralogy in the hanging wall, decreasing sharply across the PSZ to ~1.5% in the footwall. Phyllosilicates such as chlorite and

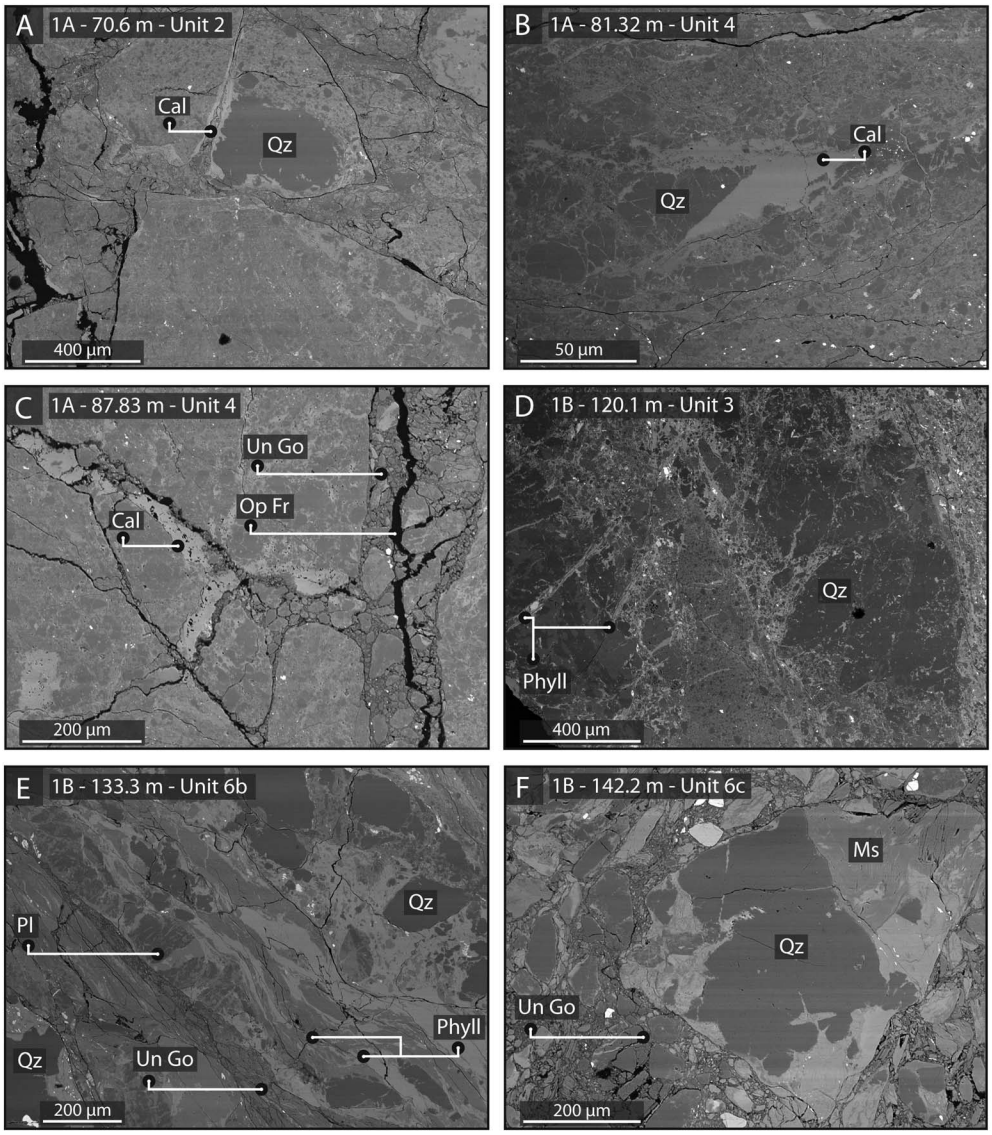

Figure 8. Backscatter electron images of (a–d) hanging wall and (e and f) footwall cataclasites. Mineral abbreviations after *Whitney and Evans* [2010]; additionally, Op Fr = open fracture, Un Go = unconsolidated gouge, Phyll = phyllosilicate. Figures 8a–8c exhibit carbonate filled veins; Figures 8c, 8e, and 8f exhibit unconsolidated gouge-filled fractures; Figure 8d contains with clay-filled fractures.

biotite are present throughout the fault zone, while smectite, an authigenic swelling clay, appears only within the PSZs.

4. Discussion

The temporal and spatial variations of permeability and seismic velocity within fault zones are thought to be largely influenced by the variation of fracture density with respect to the fault zone [*Faulkner et al.*, 2003; *Mitchell and Faulkner*, 2008, 2012]. This picture is complicated when lithological variation occurs with the fault zone [e.g., *Wibberley and Shimamoto*, 2002] and also when mineralization occurs within both the damage zone and fault core. Mineralization can occur in two ways: as authigenic mineral growth that produces clay mineral formation and as precipitation that may, respectively, heal and seal the fault [*Madariaga et al.*, 1998; *Tenthorey and Cox*, 2006]. In this section, we consider how mineralogical and microstructural characteristics influence the fault zone physical properties, how the Alpine Fault Zone compares with other mature

fault zones, and finally, how mineralogy and microstructure influence earthquake processes such as thermal pressurization and the propagation of seismic waves.

4.1. Microstructural Controls on Physical Properties

Other than a few discrete features such as the PSZ and pseudotachylyte veins, the bulk mineralogy remains largely consistent across the fault zone [*Toy et al.*, 2015; *Boulton et al.*, 2017]. Hence, the bulk mineralogy does not appear to be a major factor controlling the observed variations in physical properties. Consequently, the fracture density might be considered to be the primary influence on the physical properties at the scale of the experimental measurements. As fractures make up proportionally far less of the bulk rock than the matrix, the small variations of mineralogy associated with fractures, primarily carbonate and phyllosilicate fill, are masked by the bulk rock mineralogy in regard to seismic velocities. However, small variations in the overall mineralogy, due to fracture infill, could significantly modify the fluid transport properties of the fractures and hence those of the bulk rock.

Williams et al. [2016], using combined CT and SEM analyses of the DFDP core, to a fracture aperture resolution of >1 mm, discovered that, within the alteration zone, the majority of the fault damage is cemented with varying carbonate, clay, and gouge materials (72% being fully sealed and an additional 24% remaining partially sealed). Outside of the alteration zone (<50 m away from the PSZ), fault damage may persist between periods of seismicity, as evidenced by the high in situ permeability measured during wireline slug tests and the lack of intact core recovery outside of the alteration zone due to disaggregation [*Sutherland et al.*, 2012]. Fracture porosity is likely to be the main control of fluid flow in these damage zone ultramylonites and cataclasites, as the intact protolith or cemented regions have very low permeabilities, below the capabilities of measurement of the experimental apparatus detailed above, at $<10^{-22}$ m^2 as measured in the protolith lithologies in this study. The length scales of the fractures within a rock mass have great influence on permeability and seismic wave velocities; this scale effect is detailed in *Brace et al.* [1968] and *Nara et al.* [2011] regarding permeability and *Budiansky and O'connell* [1976] regarding seismic velocities. Samples prepared for this study were actively chosen away from the macroscopic fractures described by *Williams et al.* [2016] in order to avoid sample failure during preparation. With this in mind, the measurements reported here represent the intact matrix properties of the fault lithologies, giving the minimum permeability and maximum seismic velocity values of the Alpine Fault due to the fine-scale sampling bias inherent in this study, where heterogeneity of microstructure is a key characteristic of all fault rocks analyzed. In the following section, the nature of the fracture networks and their fillings present in the experimental samples are explored.

Open fractures within core material are predominantly opened along preexisting gouge-filled or carbonate-filled fractures, as visible in Figures 8c and 8e. These are presumably stress-relief fractures, opened during core retrieval, handling and resting prior to testing and microstructural analysis preparation. This is supported through the lack of displacement on the fracture or mobilization of the fracture fill, indicating that the fractures have opened up by dilation in "dry" conditions. As illustrated in section 3.1, there is a significant initial drop in permeability and increase in seismic velocity after an initial pressure interval between 5 and 40 MPa, after which trends in the data remain largely constant, marking the closure of open fractures and voids and allowing a more representative measurement for the specimen to be taken [*Nara et al.*, 2011].

Immediately after a seismic event, it is possible that the permeability within the fault damage zone is enhanced by 3–8 orders of magnitude [*Miller et al.*, 2004; *Mitchell and Faulkner*, 2008; *Gomila et al.*, 2016]. This transiently enhanced fluid mobility coupled with reduced grain size via cataclasis can result in a period of heightened fluid-rock interaction. *Warr and Cox* [2001] determined two generations of phyllosillicates on the Alpine Fault, hydrous chloritization at ~320°C, followed by the generation of swelling clays at shallower depths and temperatures of ~120°C. The dominant clay phases within the Alpine fault hanging wall are white mica (illite/muscovite) and chlorite [*Boulton et al.*, 2012, 2017; *Schleicher et al.*, 2015]. *Schleicher et al.* [2015] found that enhanced levels of authigenic illite and smectite are present in the PSZ in contrast to higher levels of metamorphic illite/muscovite in surrounding cataclasites. White mica and chlorite fill a large proportion of fractures in the hanging wall, while smectite is found solely in the brown PSZ fault gouges, generated from the low-temperature alteration of illite/muscovite and chlorite, which is further altered into kaolinite and goethite [*Craw*, 1984; *Boulton et al.*, 2012, 2017; *Schleicher et al.*, 2015], with the combination of ultracomminuted grains and swelling clays on the PSZ reducing permeability to ~10^{-20} to 10^{-21} m^2, becoming a hydraulic seal.

The nature of carbonate precipitation is variable, occurring as veins both parallel and cross-cutting foliation, bounding gouge-filled fractures, disseminated cement in gouge-filled fractures and fragmented clasts within gouge and cataclasite. Hanging wall cataclasites contain a pervasive carbonate infill and, as a result, are more cohesive than the carbonate-poor footwall cataclasites, resulting in the increase in permeability with distance from the PSZ into the footwall (Figure 6d).The presence of calcite networks indicates periods of damage-enhanced fluid transport focused within the hanging wall cataclasites and ultramylonites. Mineralization effectively "seals" the newly formed postseismic fracture networks, resulting in an increase in strength and stiffness relative to its immediate postrupture state and lowering of permeability of the fault zone lithologies [*Lund Snee et al.*, 2014]. Similar processes are inferred to take place in geothermal fields, with mineral precipitation reducing permeability potentially on the time scale of days for mm-scale fractures in high temperature settings, especially if considerable fluid pressure fluctuation occurs [*Griffiths et al.*, 2016; *McNamara et al.*, 2016].

A main control on the anisotropy of physical properties is the presence or lack thereof of a tectonic foliation [*Okaya et al.*, 1995; *Okaya and Christensen*, 2002]. For instance, the poorly developed fabric in the PSZ gouge exhibits the least anisotropy, while distinctly foliated specimens such as 1A-83.2 exhibit a strong anisotropy, with higher seismic wave velocity and permeability parallel to foliation and slower values perpendicular to the foliation (Figures 6 and 7). However, the nature of the cataclastic fabrics within the alteration/damage zone is spatially variable, with pods of intensely foliated material (1B-133.3) located within wide swath of unfoliated material (1B-142) or vice versa (Figures 2e and 2f and 8e and 8f). With this in mind, the experimental results from this study place a lower limit on matrix permeability and an upper limit on matrix seismic wave velocity, respectively, through the Alpine Fault. Overall, both permeability and seismic velocity anisotropy show a general trend to decreasing toward the principal slip zones, in both DFDP-1A and 1B.

4.2. Correlation With Other Studies

Figures 6b and 6e show the DFDP-1 wireline logs as a black trace in comparison to the results presented here. As each test specimen was precompacted to 105 MPa P_{eff}, it is not possible to make a direct comparison to measurements made at pressure conditions within the DFDP-1 borehole. Furthermore, the sampling length scale for the *P* wave velocity wireline tool (a single source, dual receiver logging sonde as documented in *Townend et al.* [2013]) used to collect V_p data is 304.8 mm, approximately 20 times the length of the experimental specimens used in this study. The selection of samples and subsequent sample preparation means that measurements were made on coherent core material that was perhaps more intact than the in situ material. Large, relative to specimen size, throughgoing fractures may not have been sampled in the experiments, and hence, measurements provide a minimum value of permeability and a maximum value of seismic velocity. However, the trends of the data show a reasonable comparison, indicating that the measurements made here may be representative of the permeability and seismic velocity at greater depths, equivalent to the effective pressures used in the experiments. Slug tests performed in the distal damage zone of DFDP-1 recorded in situ permeability of 10^{-14} m^2, indicating that permeability may drop by up to 5 orders of magnitude at low effective pressures toward the fault core [*Sutherland et al.*, 2012].

Carpenter et al. [2014], illustrated in Figures 6b and 6e, presented similar laboratory measurements of DFDP-1 fault rock permeability and seismic velocity, but at a lower P_{eff} range (2.5–65 MPa) with no preconsolidation. The permeability data presented in this study correlate with *Carpenter et al.*'s [2014] data, with measurement ranges overlapping at similar depths in the core. In terms of seismic velocity, the data presented here are higher than those in *Carpenter et al.* [2014]. This is most likely due to preconsolidation of samples in the method used here, and therefore, the values for seismic velocity are more representative of those at greater depth than the data of *Carpenter et al.* [2014]. Other factors that might produce differences are the variation in specimen dimensions, frequency, and natural specimen variation.

The overall variations in seismic velocities with depth in this study and that of *Carpenter et al.* [2014] correlate well with each other (Figures 6b and 6e). The PSZ exhibits lower velocities than the surrounding cataclasites, and the higher velocities witnessed in the hanging wall cataclasites in contrast to the footwall are indicative of a greater degree of carbonate cementation and cohesiveness and potentially asymmetrical damage imparted upon the fault zone during seismicity [*Townend et al.*, 2013].

Physical property measurements of the Alpine Fault Zone are consistent with a number of mature, geochemically altered fault zones worldwide. Similarities with studies performed on the Nojima Fault Zone [*Mizoguchi et al.*, 2008], Median Tectonic Line (MTL) [*Wibberley and Shimamoto*, 2002], the San Andreas Fault [*Morrow et al.*, 2014], and the Carboneras Fault [*Faulkner et al.*, 2003] highlight the microstructural complexity within a fault damage zone, with numerous episodes of brittle rupture damage and subsequent fluid-rock interactions. Laboratory gas permeability measurements of the MTL fault core show values between 10^{-13} and 10^{-21} m^2 (P_{eff} = 50–180 MPa) that are attributed to enhanced grain size reduction with increasing proximity to the PSZ [*Wibberley and Shimamoto*, 2002]. Material reclaimed from depth on the actively creeping segment of the San Andreas Fault shows a similar range of permeabilities of 10^{-18} to 10^{-23} m^2 (P_{eff} = 10–120 MPa), with gouge material exhibiting lower permeabilities than bounding cataclasites [*Morrow et al.*, 2014]. The gouge zones of the Carboneras Fault show permeability values in the range of 10^{-17} to 10^{-22} m^2, with permeability anisotropy of up to 3 orders of magnitude [*Faulkner and Rutter*, 2000; *Faulkner et al.*, 2003].

The permeability variations of up to 6 orders of magnitude in previous studies seem typical of major, mature fault zones and are related directly to degree of comminution and associated authigenic mineral generation and cementation. Both experimental and in situ seismic velocity measurements have revealed that faults, and their associated damage zones are regions of low seismic velocities [*Mooney and Ginzburg*, 1986; *Li et al.*, 2004; *Jeppson et al.*, 2010; *Jeppson and Tobin*, 2015], which concur with velocity measurements in this study.

4.3. Implications for Fault Zone Properties During the Seismic Cycle

The hydraulic properties of fault rock have implications for transient variations in pore fluid behavior during seismic slip. Coseismic thermal effects may promote slip propagation via processes such as thermal pressurization [*Rempel and Rice*, 2006; *Rice*, 2006]. The low permeability of the core of the Alpine Fault and alteration zone in the hanging wall may favor thermal pressurization during earthquake rupture [*Segall and Rice*, 1995; *Wibberley*, 2002; *Mizoguchi et al.*, 2008; *Leclère et al.*, 2015]. Evidence for the development of overpressures within the damage/alteration zone includes gouge-filled fractures emanating from, and propagating through, the PSZ. These features indicate that dilatancy-driven pore depressurization may also stabilize slip and arrest rupture [*Segall and Rice*, 1995; *Samuelson et al.*, 2009].

Geochemical studies of vein mineralization [*Menzies et al.*, 2014] and fluids from hot springs from the Alpine Fault hanging wall [*Barnes et al.*, 1978] show that much of the fluid circulating at $<$2 km depth are meteorically derived. Fluid inclusion measurements indicate that water infiltration is at least 2 orders of magnitude greater than metamorphic water production [*Menzies et al.*, 2016]. In its low permeability prerupture state the Alpine fault appears to act as a barrier to fluid flow, isolating fluid geochemical regimes on a regional scale. Similarities can be drawn with low fluid $^3He/^4He$ ratios in San Andreas Fault fluids at seismogenic depths, indicating a dominantly meteorically derived source. As the overall permeability structure across the creeping sections of the San Andreas is low, it has been suggested that the proportion of mantle-derived fluids will increase within more permeable faults at distance from the active San Andreas strands within the North American Plate [*Wiersberg and Erzinger*, 2007].

The strong, penetrative tectonic and metamorphic foliations present in the protolith host-rock bounding the Alpine Fault, the hanging wall Alpine Schist and mylonite sequence lithologies, have a strong regional seismic anisotropy [*Christensen and Okaya*, 2007]. This anisotropy extends to depths of $<$90 km into the deep lithosphere and is broadly distributed, according to shear wave splitting studies [*Karalliyadda and Savage*, 2013]. Fault Zone Guided Waves (FZGWs) have been observed on the Alpine Fault, in which seismic waves are channeled and propagated along the fault zone [*Eccles et al.*, 2015]. These FZGWs occur due to material contrast between the fault zone material and the intact country rock, causing seismic waves to focus along low-velocity zones. Our observations of fault zone velocities in comparison to the intact country rock are consistent with the presence of these FZGWs. These types of seismic wave allow the fault to be imaged and some of the properties of the fault at depth, such as fault zone width, to be inferred [*Li et al.*, 1997; *Ben-Zion*, 1998]. The use of FZGWs is critically dependent on the velocity contrast between the fault and the country rock and the orientation of any anisotropic fabric in the country rock. If the slow direction of any anisotropy is oriented perpendicular to the low-velocity fault zone, seismic energy may escape the low-velocity zone, making the fault difficult to recognize through FZGWs [*Kelly et al.*, 2017]. The seismic velocities and anisotropies reported in this study support previous regional observations on the behavior

of seismic waves on the Alpine Fault, where the fault core material has lower seismic velocities than the fastest direction in the country rock hosting it and the heterogeneity of microstructures within the fault zone serves to homogenize any anisotropy [*Eccles et al.*, 2015].

5. Conclusion

Our suite of experimental measurements shows a zone of low permeability and low seismic velocity material bounding the PSZ of the Central Alpine Fault, under conditions approximating depths of 5–6 km. Measurements performed on protolith lithologies show lower permeabilities and higher seismic velocities than the fault-damaged rock owing to their intact, unfractured nature. Low permeabilities at low experimental pressures are explained by the presence of fine grained alteration products and carbonate precipitation within the fracture networks of the fault hanging wall. The PSZ, being composed of ultra-fine grained alteration products, acts as a barrier to cross-fault fluid flow postseismicity. This is in agreement with other petrophysical studies on other mature faults subjected to extensive comminution and fluid-rock alteration [*Wibberley and Shimamoto*, 2002; *Faulkner et al.*, 2003; *Boulton et al.*, 2012; *Townend et al.*, 2013; *Carpenter et al.*, 2014; *Morrow et al.*, 2014].

The evolution of fault rock microstructure with seismic shear and subsequent interseismic fluid-rock interaction has a great effect on the hydraulic and elastic properties of fault zones. This evolution is complex and cyclical, potentially promoting rupture via dynamic coseismic processes such as thermal pressurization and dilatancy hardening. During interseismic periods, fluid flow is likely concentrated upon pervasive, unconsolidated gouge-filled fracture networks that are progressively mineralized/altered, reducing along-fault communication of pore fluid. With fluid focusing along these fracture networks, fault rock fabrics have little influence on permeability anisotropy. In addition, as the cataclastic microstructures are so variable on a mm-cm scale, their overall effect within the fault zone would be to homogenize seismic velocities, limiting seismic anisotropy. The main microstructural controls on fault rock physical properties are throughgoing fractures, both gouge-filled and mineralized, which have a great effect on seismic wave speeds and fluid flow at the experimental specimen scale and likely to act as preferential fluid flow paths and planes of discontinuity in the Alpine Fault Zone as a whole.

Acknowledgments
This work was supported by Natural Environment Research Council grants NE/H012486/1 and NE/J024449/1. We would like to thank all those involved in and who made possible the Deep Fault Drilling Project (DFDP-1) as well as Gary Coughlan, Henri Leclère, Carmel Pinnington, and Paul Hands for technical assistance during this study. We would also like to thank Ludmila Adams and Auke Baarnhorn (University of Auckland, New Zealand and Delft University of Technology, Netherlands) for performing the nanoCT scans at the Delft University of Technology, Netherlands, detailed in the supporting information.

References

Anders, M. H., and D. V. Wiltschko (1994), Microfracturing, paleostress and the growth of faults, *J. Struct. Geol.*, *16*(6), 795–815, doi:10.1016/0191-8141(94)90146-5.

Barnes, I., C. J. Downes, and J. R. Hulston (1978), Warm springs, South Island, New Zealand, and their potentials to yield laumontite, *Am. J. Sci.*, *278*(10), 1412–1427, doi:10.2475/ajs.278.10.1412.

Ben-Zion, Y. (1998), Properties of seismic fault zone waves and their utility for imaging low-velocity structures, *J. Geophys. Res.*, *103*(B6), 12,567–12,585, doi:10.1029/98JB00768.

Bernabe, Y. (1987), The effective pressure law for permeability during pore pressure and confining pressure cycling of several crystalline rocks, *J. Geophys. Res.*, *92*(B1), 649–657, doi:10.1029/JB092iB01p00649.

Birch, F. (1960), The velocity of compressional waves in rocks to 10 kilobars: 1, *J. Geophys. Res.*, *65*(4), 1083–1102, doi:10.1029/JZ065i004p01083.

Boulton, C., B. M. Carpenter, V. Toy, and C. Marone (2012), Physical properties of surface outcrop cataclastic fault rocks, Alpine Fault, New Zealand, *Geochem. Geophys. Geosyst.*, *13*, Q01018, doi:10.1029/2011GC003872.

Boulton, C., D. E. Moore, D. A. Lockner, V. G. Toy, J. Townend, and R. Sutherland (2014), Frictional properties of exhumed fault gouges in DFDP-1 cores, Alpine Fault, New Zealand, *Geophys. Res. Lett.*, *41*, 356–362, doi:10.1002/2013GL058236.

Boulton, C., C. D. Menzies, V. G. Toy, J. Townend, and R. Sutherland (2017), Geochemical and microstructural evidence for interseismic changes in fault zone permeability and strength, Alpine Fault, New Zealand, *Geochem. Geophys. Geosyst.*, *18*, 238–265, doi:10.1002/2016GC006588.

Brace, W. F., J. B. Walsh, and W. T. Frangos (1968), Permeability of granite under high pressure, *J. Geophys. Res.*, *73*(6), 2225–2236, doi:10.1029/JB073i006p02225.

Budiansky, B., and R. J. O'connell (1976), Elastic moduli of a cracked solid, *Int. J. Solids Struct.*, *12*(2), 81–97, doi:10.1016/0020-7683(76)90044-5.

Caine, J. S., J. P. Evans, and C. B. Forster (1996), Fault zone architecture and permeability structure, *Geology*, *24*(11), 1025–1028, doi:10.1130/0091-7613(1996)024<1025:FZAAPS>2.3.CO;2.

Carpenter, B. M., H. Kitajima, R. Sutherland, J. Townend, V. G. Toy, and D. M. Saffer (2014), Hydraulic and acoustic properties of the active Alpine Fault, New Zealand: Laboratory measurements on DFDP-1 drill core, *Earth Planet. Sci. Lett.*, *390*, 45–51.

Chester, F. M., and J. M. Logan (1986), Implications for mechanical properties of brittle faults from observations of the Punchbowl fault zone, California, *Pure Appl. Geophys.*, *124*(1), 79–106, doi:10.1007/BF00875720.

Christensen, N. I., and D. A. Okaya (2007), Compressional and shear wave velocities in South Island, New Zealand rocks and their application to the interpretation of seismological models of the New Zealand crust, in *A Continental Plate Boundary: Tectonics at South Island, New Zealand*, pp. 123–155, AGU, Wahington D. C.

Cooper, A. F. (1972), Progressive metamorphism of metabasic rocks from the haast schist group of Southern New Zealand, *J. Petrol.*, *13*(3), 457–492, doi:10.1093/petrology/13.3.457.

Craw, D. (1984), Ferrous-iron-bearing vermiculite-smectite series formed during alteration of chlorite to kaolinite, Otago Schist, New Zealand, *Clay Miner.*, *19*(4), 509–520.

Cross, A. J., S. Kidder, and D. J. Prior (2015), Using microstructures and TitaniQ thermobarometry of quartz sheared around garnet porphyroclasts to evaluate microstructural evolution and constrain an Alpine Fault Zone geotherm, *J. Struct. Geol.*, *75*, 17–31, doi:10.1016/j.jsg.2015.02.012.

De Pascale, G. P., and R. M. Langridge (2012), New on-fault evidence for a great earthquake in A.D. 1717, central Alpine Fault, New Zealand, *Geology*, *40*(9), 791–794, doi:10.1130/G33363.1.

Eberhart-Phillips, D., and S. Bannister (2002), Three-dimensional crustal structure in the Southern Alps region of New Zealand from inversion of local earthquake and active source data, *J. Geophys. Res.*, *107*(B10), 2262, doi:10.1029/2001JB000567.

Eberhart-Phillips, D. (1995), Examination of seismicity in the central Alpine Fault region, South Island, New Zealand, *N. Z. J. Geol. Geophys.*, *38*(4), 571–578, doi:10.1080/00288306.1995.9514685.

Eccles, J. D., A. K. Gulley, P. E. Malin, C. M. Boese, J. Townend, and R. Sutherland (2015), Fault zone guided wave generation on the locked, late interseismic Alpine Fault, New Zealand, *Geophys. Res. Lett.*, *42*, 5736–5743, doi:10.1002/2015GL064208.

Evans, J. P., C. B. Forster, and J. V. Goddard (1997), Permeability of fault-related rocks, and implications for hydraulic structure of fault zones, *J. Struct. Geol.*, *19*(11), 1393–1404, doi:10.1016/S0191-8141(97)00057-6.

Farrell, N. J. C., D. Healy, and C. W. Taylor (2014), Anisotropy of permeability in faulted porous sandstones, *J. Struct. Geol.*, *63*, 50–67, doi:10.1016/j.jsg.2014.02.008.

Faulkner, D. R., and P. J. Armitage (2013), The effect of tectonic environment on permeability development around faults and in the brittle crust, *Earth Planet. Sci. Lett.*, *375*, 71–77.

Faulkner, D. R., and E. H. Rutter (1998), The gas permeability of clay-bearing fault gouge at 20°C, *Geol. Soc. Lond. Spec. Publ.*, *147*(1), 147–156, doi:10.1144/GSL.SP.1998.147.01.10.

Faulkner, D. R., and E. H. Rutter (2000), Comparisons of water and argon permeability in natural clay-bearing fault gouge under high pressure at 20°C, *J. Geophys. Res.*, *105*(B7), 16,415–16,426, doi:10.1029/2000JB900134.

Faulkner, D. R., A. Lewis, and E. H. Rutter (2003), On the internal structure and mechanics of large strike-slip fault zones: Field observations of the Carboneras fault in southeastern Spain, *Tectonophysics*, *367*(3), 235–251, doi:10.1016/S0040-1951(03)00134-3.

Faulkner, D. R., T. M. Mitchell, E. H. Rutter, and J. Cembrano (2008), On the structure and mechanical properties of large strike-slip faults, *Geol. Soc. Lond. Spec. Publ.*, *299*(1), 139–150, doi:10.1144/SP299.9.

Faulkner, D. R., C. A. L. Jackson, R. J. Lunn, R. W. Schlische, Z. K. Shipton, C. A. J. Wibberley, and M. O. Withjack (2010), A review of recent developments concerning the structure, mechanics and fluid flow properties of fault zones, *J. Struct. Geol.*, *32*(11), 1557–1575, doi:10.1016/j.jsg.2010.06.009.

Fortin, J., S. Stanchits, S. Vinciguerra, and Y. Guéguen (2011), Influence of thermal and mechanical cracks on permeability and elastic wave velocities in a basalt from Mt. Etna volcano subjected to elevated pressure, *Tectonophysics*, *503*(1–2), 60–74, doi:10.1016/j.tecto.2010.09.028.

Gomila, R., G. Arancibia, T. M. Mitchell, J. M. Cembrano, and D. R. Faulkner (2016), Palaeopermeability structure within fault-damage zones: A snap-shot from microfracture analyses in a strike-slip system, *J. Struct. Geol.*, *83*, 103–120, doi:10.1016/j.jsg.2015.12.002.

Griffiths, L., M. J. Heap, F. Wang, D. Daval, H. A. Gilg, P. Baud, J. Schmittbuhl, and A. Genter (2016), Geothermal implications for fracture-filling hydrothermal precipitation, *Geothermics*, *64*, 235–245, doi:10.1016/j.geothermics.2016.06.006.

Guéguen, Y., and J. Sarout (2011), Characteristics of anisotropy and dispersion in cracked medium, *Tectonophysics*, *503*(1), 165–172, doi:10.1016/j.tecto.2010.09.021.

Hoffmann-Rothe, A., O. Ritter, and C. Janssen (2004), Correlation of electrical conductivity and structural damage at a major strike-slip fault in northern Chile, *J. Geophys. Res.*, *109*, B10101, doi:10.1029/2004JB003030.

Holdsworth, R. E. (2004), Weak faults—Rotten cores, *Science*, *303*(5655), 181–182, doi:10.1126/science.1092491.

Jeppson, T. N., and H. J. Tobin (2015), San Andreas Fault Zone velocity structure at SAFOD at core, log, and seismic scales, *J. Geophys. Res. Solid Earth*, *120*, 4983–4997, doi:10.1002/2015JB012043.

Jeppson, T. N., K. K. Bradbury, and J. P. Evans (2010), Geophysical properties within the San Andreas Fault Zone at the San Andreas Fault Observatory at Depth and their relationships to rock properties and fault zone structure, *J. Geophys. Res.*, *115*, B12423, doi:10.1029/2010JB007563.

Karalliyadda, S. C., and M. K. Savage (2013), Seismic anisotropy and lithospheric deformation of the plate-boundary zone in South Island, New Zealand: Inferences from local *S*-wave splitting, *Geophys. J. Int.*, *193*(2), 507–530, doi:10.1093/gji/ggt022.

Kelly, C. M., D. R. Faulkner, and A. R. Rietbrock (2017), Seismically invisible fault zones: laboratory insights into imaging faults in anisotropic rocks, *Geophys. Res. Lett.*, *122*, doi:10.1002/2017GL073726.

Lamb, S., and E. Smith (2013), The nature of the plate interface and driving force of interseismic deformation in the New Zealand plate-boundary zone, revealed by the continuous GPS velocity field, *J. Geophys. Res. Solid Earth*, *118*, 3160–3189, doi:10.1002/jgrb.50221.

Lamb, S., E. Smith, T. Stern, and E. Warren-Smith (2015), Continent-scale strike-slip on a low-angle fault beneath New Zealand's Southern Alps: Implications for crustal thickening in oblique collision zones, *Geochem. Geophys. Geosyst.*, *16*, 3076–3096, doi:10.1002/2015GC005990.

Langridge, R. M., R. Basili, L. Basher, and A. P. Wells (2012), Late Holocene landscape change history related to the Alpine Fault determined from drowned forests in Lake Poerua, Westland, New Zealand, *Nat. Hazards Earth Syst. Sci.*, *12*(6), 2051–2064, doi:10.5194/nhess-12-2051-2012.

Lay, V., S. Buske, A. Lukács, A. R. Gorman, S. Bannister, and D. R. Schmitt (2016), Advanced seismic imaging techniques characterize the Alpine Fault at Whataroa (New Zealand), *J. Geophys. Res. Solid Earth*, *121*, 8792–8812, doi:10.1002/2016JB013534.

Leclère, H., F. Cappa, D. Faulkner, O. Fabbri, P. Armitage, and O. Blake (2015), Development and maintenance of fluid overpressures in crustal fault zones by elastic compaction and implications for earthquake swarms, *J. Geophys. Res. Solid Earth*, *120*, 4450–4473, doi:10.1002/2014JB011759.

Li, Y. G., W. L. Ellsworth, C. H. Thurber, P. E. Malin, and K. Aki (1997), Fault-zone guided waves from explosions in the San Andreas Fault at Parkfield and Cienega Valley, California, *Bull. Seismol. Soc. Am.*, *87*(1), 210–221.

Li, Y. G., J. E. Vidale, and E. S. Cochran (2004), Low-velocity damaged structure of the San Andreas Fault at Parkfield from fault zone trapped waves, *Geophys. Res. Lett.*, *31*, L12S06, doi:10.1029/2003GL019044.

Little, T. A., R. J. Holcombe, and B. R. Ilg (2002), Kinematics of oblique collision and ramping inferred from microstructures and strain in middle crustal rocks, Central Southern Alps, New Zealand, *J. Struct. Geol.*, *24*(1), 219–239, doi:10.1016/S0191-8141(01)00060-8.

Little, T. A., D. J. Prior, V. G. Toy, and Z. R. Lindroos (2015), The link between strength of lattice preferred orientation, second phase content and grain boundary migration: A case study from the Alpine Fault Zone, New Zealand, *J. Struct. Geol.*, *81*, 59–77, doi:10.1016/j.jsg.2015.09.004.

Lund Snee, J.-E., V. G. Toy, and K. Gessner (2014), Significance of brittle deformation in the footwall of the Alpine Fault, New Zealand: Smithy Creek Fault zone, *J. Struct. Geol.*, *64*, 79–98, doi:10.1016/j.jsg.2013.06.002.

Madariaga, R., K. Olsen, and R. Archuleta (1998), Modeling dynamic rupture in a 3D earthquake fault model, *Bull. Seismol. Soc. Am.*, *88*(5), 1182–1197.

Mainprice, D., and M. Humbert (1994), Methods of calculating petrophysical properties from lattice preferred orientation data, *Surv. Geophys.*, *15*(5), 575–592, doi:10.1007/BF00690175.

McNamara, D. D., A. Lister, and D. J. Prior (2016), Calcite sealing in a fractured geothermal reservoir: Insights from combined EBSD and chemistry mapping, *J. Volcanol. Geotherm. Res.*, *323*, 38–52, doi:10.1016/j.jvolgeores.2016.04.042.

Menzies, C. D., D. A. H. Teagle, D. Craw, S. C. Cox, A. J. Boyce, C. D. Barrie, and S. Roberts (2014), Incursion of meteoric waters into the ductile regime in an active orogen, *Earth Planet. Sci. Lett.*, *399*, 1–13, doi:10.1016/j.epsl.2014.04.046.

Menzies, C. D., D. A. H. Teagle, S. Niedermann, S. C. Cox, D. Craw, M. Zimmer, M. J. Cooper, and J. Erzinger (2016), The fluid budget of a continental plate boundary fault: Quantification from the Alpine Fault, New Zealand, *Earth Planet. Sci. Lett.*, *445*, 125–135, doi:10.1016/j.epsl.2016.03.046.

Miller, S. A., C. Collettini, L. Chiaraluce, M. Cocco, M. Barchi, and B. J. P. Kaus (2004), Aftershocks driven by a high-pressure CO_2 source at depth, *Nature*, *427*(6976), 724–727.

Mitchell, T. M., and D. R. Faulkner (2008), Experimental measurements of permeability evolution during triaxial compression of initially intact crystalline rocks and implications for fluid flow in fault zones, *J. Geophys. Res.*, *113*, B11412, doi:10.1029/2008JB005588.

Mitchell, T. M., and D. R. Faulkner (2009), The nature and origin of off-fault damage surrounding strike-slip fault zones with a wide range of displacements: A field study from the Atacama fault system, northern Chile, *J. Struct. Geol.*, *31*(8), 802–816, doi:10.1016/j.jsg.2009.05.002.

Mitchell, T. M., and D. R. Faulkner (2012), Towards quantifying the matrix permeability of fault damage zones in low porosity rocks, *Earth Planet. Sci. Lett.*, *339–340*, 24–31, doi:10.1016/j.epsl.2012.05.014.

Mizoguchi, K., T. Hirose, T. Shimamoto, and E. Fukuyama (2008), Internal structure and permeability of the Nojima fault, southwest Japan, *J. Struct. Geol.*, *30*(4), 513–524, doi:10.1016/j.jsg.2007.12.002.

Mooney, W. D., and A. Ginzburg (1986), Seismic measurements of the internal properties of fault zones, *Pure Appl. Geophys. PAGEOPH*, *124*(1–2), 141–157, doi:10.1007/BF00875723.

Morrow, C. A., D. A. Lockner, D. E. Moore, and S. Hickman (2014), Deep permeability of the San Andreas Fault from San Andreas Fault Observatory at Depth (SAFOD) core samples, *J. Struct. Geol.*, *64*, 99–114, doi:10.1016/j.jsg.2013.09.009.

Nara, Y., P. G. Meredith, T. Yoneda, and K. Kaneko (2011), Influence of macro-fractures and micro-fractures on permeability and elastic wave velocities in basalt at elevated pressure, *Tectonophysics*, *503*(1–2), 52–59, doi:10.1016/j.tecto.2010.09.027.

Norris, R. J., and A. F. Cooper (2001), Late Quaternary slip rates and slip partitioning on the Alpine Fault, New Zealand, *J. Struct. Geol.*, *23*(2–3), 507–520, doi:10.1016/S0191-8141(00)00122-X.

Norris, R. J., and V. G. Toy (2014), Continental transforms: A view from the Alpine Fault, *J. Struct. Geol.*, *64*, 3–31, doi:10.1016/j.jsg.2014.03.003.

Okaya, D., N. Christensen, D. Stanley, T. Stern, and S. I. G. T. (SIGHT) W. Group (1995), Crustal anisotropy in the vicinity of the Alpine Fault Zone, South Island, New Zealand, *N. Z. J. Geol. Geophys.*, *38*(4), 579–583, doi:10.1080/00288306.1995.9514686.

Okaya, D. A., and N. I. Christensen (2002), Anisotropic effects of non-axial seismic wave propagation in foliated crustal rocks, *Geophys. Res. Lett.*, *29*(11), 1507, doi:10.1029/2001GL014285.

Rempel, A. W., and J. R. Rice (2006), Thermal pressurization and onset of melting in fault zones, *J. Geophys. Res.*, *111*, B09314, doi:10.1029/2006JB004314.

Rice, J. R. (2006), Heating and weakening of faults during earthquake slip, *J. Geophys. Res.*, *111*, B05311, doi:10.1029/2005JB004006.

Rice, J. R., and M. P. Cleary (1976), Some basic stress diffusion solutions for fluid-saturated elastic porous media with compressible constituents, *Rev. Geophys.*, *14*(2), 227–241, doi:10.1029/RG014i002p00227.

Rietbrock, A. (2001), *P* wave attenuation structure in the fault area of the 1995 Kobe earthquake, *J. Geophys. Res.*, *106*(B3), 4141–4154, doi:10.1029/2000JB900234.

Samuelson, J., D. Elsworth, and C. Marone (2009), Shear-induced dilatancy of fluid-saturated faults: Experiment and theory, *J. Geophys. Res.*, *114*, B12404, doi:10.1029/2008JB006273.

Sato, H., M. C. Fehler, and T. Maeda (2012), *Seismic Wave Propagation and Scattering in the Heterogeneous Earth: Second Edition*, Springer, Berlin.

Schleicher, A. M., R. Sutherland, J. Townend, V. G. Toy, and B. van der Pluijm (2015), Clay mineral formation and fabric development in the DFDP-1B borehole, central Alpine Fault, New Zealand, *N. Z. J. Geol. Geop.*, *58*(1), 13–21, doi:10.1080/00288306.2014.979841.

Segall, P., and J. R. Rice (1995), Dilatancy, compaction, and slip instability of a fluid-infiltrated fault, *J. Geophys. Res.*, *100*(B11), 22,155–22,171, doi:10.1029/95JB02403.

Sibson, R. H., S. H. White, and B. K. Atkinson (1981), Structure and distribution of fault rocks in the Alpine Fault Zone, New Zealand, *Geol. Soc. Lond. Spec. Publ.*, *9*(1), 197–210, doi:10.1144/GSL.SP.1981.009.01.18.

Sutherland, R., et al. (2007), Do great earthquakes occur on the Alpine Fault in Central South Island, New Zealand? *A Cont. Plate Bound. Tectonics South Island, N. Z.*, 235–251, doi:10.1029/175GM12.

Sutherland, R., et al. (2011), *Operations and Well Completion Report for Boreholes DFDP-1A and DFDP-1B*, Deep Fault Drill. Project, Alpine Fault, Gaunt Creek, New Zealand, Lower Hutt, NZ.

Sutherland, R., et al. (2012), Drilling reveals fluid control on architecture and rupture of the Alpine Fault, New Zealand, *Geology*, *40*(12), 1143–1146, doi:10.1130/G33614.1.

Sutherland, R., et al. (2017), Extreme hydrothermal conditions at an active plate-bounding fault, *Nature*, *546*(7656), 137–140.

Tenthorey, E., and S. F. Cox (2006), Cohesive strengthening of fault zones during the interseismic period: An experimental study, *J. Geophys. Res.*, *111*, B09202, doi:10.1029/2005JB004122.

Townend, J., R. Sutherland, V. G. Toy, J. D. Eccles, C. Boulton, S. C. Cox, and D. McNamara (2013), Late-interseismic state of a continental plate-bounding fault: Petrophysical results from DFDP-1 wireline logging and core analysis, Alpine Fault, New Zealand, *Geochem. Geophys. Geosyst.*, *14*, 3801–3820, doi:10.1002/ggge.20236.

Toy, V. G., D. Craw, A. F. Cooper, and R. J. Norris (2010), Thermal regime in the central Alpine Fault Zone, New Zealand: Constraints from microstructures, biotite chemistry and fluid inclusion data, *Tectonophysics*, *485*(1–4), 178–192, doi:10.1016/j.tecto.2009.12.013.

Toy, V. G., et al. (2015), Fault rock lithologies and architecture of the central Alpine Fault, New Zealand, revealed by DFDP-1 drilling, *Lithosphere*, *7*(2), 155–173, doi:10.1130/l395.1.

Warr, L. N., and S. Cox (2001), Clay mineral transformations and weakening mechanisms along the Alpine Fault, New Zealand, *Geol. Soc. Lond. Spec. Publ.*, *186*(1), 85–101, doi:10.1144/GSL.SP.2001.186.01.06.

Whitney, D. L., and B. W. Evans (2010), Abbreviations for names of rock-forming minerals, *Am. Mineral.*, *95*(1), 185–187, doi:10.2138/am.2010.3371.

Wibberley, C. A. J. (2002), Hydraulic diffusivity of fault gouge zones and implications for thermal pressurization during seismic slip, *Earth, Planets Space*, *54*(11), 1153–1171, doi:10.1186/BF03353317.

Wibberley, C. A. J., and T. Shimamoto (2002), Internal structure and permeability of major strike-slip fault zones: The Median Tectonic Line in Mie Prefecture, Southwest Japan, *J. Struct. Geol.*, *25*(1), 59–78, doi:10.1016/S0191-8141(02)00014-7.

Wiersberg, T., and J. Erzinger (2007), A helium isotope cross-section study through the San Andreas Fault at seismogenic depths, *Geochem. Geophys. Geosyst.*, *8*, Q01002, doi:10.1029/2006GC001388.

Williams, J. N., V. G. Toy, C. Massiot, D. D. McNamara, and T. Wang (2016), Damaged beyond repair? Characterising the damage zone of a fault late in its interseismic cycle, the Alpine Fault, New Zealand, *J. Struct. Geol.*, *90*, 76–94, doi:10.1016/j.jsg.2016.07.006.

Wilson, J. E., J. S. Chester, and F. M. Chester (2003), Microfracture analysis of fault growth and wear processes, Punchbowl Fault, San Andreas system, California, *J. Struct. Geol.*, *25*(11), 1855–1873, doi:10.1016/S0191-8141(03)00036-1.

Wintsch, R. P., R. Christoffersen, and A. K. Kronenberg (1995), Fluid-rock reaction weakening of fault zones, *J. Geophys. Res.*, *100*(B7), 13,021–13,032, doi:10.1029/94JB02622.

Zoback, M., S. Hickman, W. Ellsworth, and S. S. Team (2011), Scientific drilling into the San Andreas Fault Zone—An overview of SAFOD's first five years, *Sci. Drill.*, *11*, 14–28, doi:10.2204/iodp.sd.11.02.2011.